ISSN: 1692-7257 - Volume 1 – Number 47 - 2026

RCTA
Revista Colombiana de Tecnologías de Avanzada
UNIPAMPLONA

Digital Object Identifier: 10.24054/rcta.v1i47.4108

Identification of asbestos-cement in NIR images via spectral similarity and artificial neural networks

Identificación de asbesto-cemento en imágenes NIR mediante métodos de similitud espectral y redes neuronales artificiales

PhD. Gabriel Elías Chanchí Golondrino[1], PhD. Manuel Alejandro Ospina Alarcón[1], PhD. Manuel Saba[2]

[1] ***Universidad de Cartagena,*** *Facultad de Ingeniería, Prog. de Ingeniería de Sistema, Cartagena, Bolívar, Colombia.*
[2] ***Universidad de Cartagena,*** *Facultad de Ingeniería, Prog. de Ingeniería Civil, Cartagena, Bolívar, Colombia.*

Correspondence: *gchanchig@unicartagena.edu.co*

Received: *July 26, 2025.* ***Accepted:*** *December 20, 2025.* ***Published:*** *January 01, 2026.*

How to cite: *G. E. Chanchí Golondrino, M. A. Ospina Alarcón y M. Saba, "Identification of asbestos-cement in NIR images via spectral similarity and artificial neural networks", RCTA, vol. 1, n.º. 47, pp. 46-61, Jan. 2026. Recuperado de https://ojs.unipamplona.edu.co/index.php/rcta/article/view/4108*

Abstract: This study employs airborne multispectral imagery obtained from the repository of the Environmental Public Agency of Cartagena (EPA), which provides a spatial resolution of 0.17 m/pixel. The dataset consists of four spectral bands (R, G, B, and NIR), from which 300 spectral signatures of asbestos–cement roofing and 300 signatures of other materials were extracted. The labeling was conducted through visual interpretation supported by field visits. Two configurations of the data cube were evaluated: one containing the four multispectral bands and another with five bands, generated by incorporating the first principal component obtained through PCA. Three spectral similarity measures (Cosine-Based Similarity (CBS), Spectral Distance Similarity (SDS), and Euclidean Distance Similarity (EDS)) were compared along with an artificial neural network (ANN) model. The performance was assessed using a 70–30 split based on precision, recall, F1-score, and execution time. The results indicate that EDS and CBS achieved the highest detection accuracy, with EDS being computationally more efficient (CBS was 2.22 times slower). These findings demonstrate that EDS and CBS are promising methods for the efficient detection of asbestos–cement roofing from multispectral imagery and can be extrapolated to the identification of other materials under similar spatial-resolution and data-quality conditions.

Keywords: Asbestos-cement, multispectral images, spectral similarity,artificial neural networks.

Resumen: Este estudio emplea imágenes multiespectrales aéreas obtenidas a partir del repositorio del Establecimiento Público Ambiental de Cartagena (EPA), las cuales cuentan con una resolución espacial de 0.17 m/píxel. El conjunto de datos está compuesto por cuatro bandas espectrales (R, G, B y NIR), a partir de las cuales se extrajeron 300 firmas espectrales de cubiertas de asbesto-cemento y 300 firmas de otros materiales. El etiquetado se realizó mediante interpretación visual apoyada en visitas de campo. Se evaluaron dos configuraciones del cubo de datos: una con las cuatro bandas multiespectrales y otra con cinco bandas, generada mediante la incorporación del primer componente principal obtenido mediante PCA. Se compararon tres medidas de similitud espectral (Cosine-Based Similarity (CBS), Spectral Distance Similarity

(SDS) y Euclidean Distance Similarity (EDS)) junto con un modelo de red neuronal artificial (ANN). El desempeño se evaluó mediante división 70–30 utilizando métricas de precisión, recall, F1 y tiempo de ejecución. Los resultados indican que EDS y CBS alcanzaron la mayor exactitud en la detección, siendo EDS computacionalmente más eficiente (CBS fue 2,22 veces más lento). Estos hallazgos demuestran que EDS y CBS son métodos prometedores para la detección eficiente de cubiertas de asbesto-cemento a partir de imágenes multiespectrales, y pueden ser extrapolados a la identificación de otros materiales bajo condiciones similares de resolución espacial y calidad de datos.

Palabras clave: Asbesto-cemento, imágenes multiespectrales, similitud espectral, redes neuronales artificiales.

1. INTRODUCTION

Remote sensing is a technique that identifies, measures, and analyzes the characteristics of objects or areas on the Earth's surface without direct contact, by detecting and recording electromagnetic energy reflected or emitted by them [1], [2]. To achieve this, remote sensing employs sensors installed on satellites, airplanes, or drones, which operate across different parts of the electromagnetic spectrum (visible, infrared, microwave, etc.) [3], [4]. Compared to traditional methods, remote sensing offers various advantages for environmental monitoring; it allows for the monitoring of large areas of land in a short time without requiring physical contact with the study area, which facilitates continuous observation and tracking of changes over time [5]-[8].

Among the most widespread remote sensing techniques, spectral images stand out. These can be defined as images that capture information about a scene across multiple bands of the electromagnetic spectrum, allowing for the analysis of the composition and characteristics of observed objects. They are thus considered "data cubes" because they organize information in three dimensions: two spatial dimensions (x,y) and one spectral dimension (wavelength) [9]-[11]. Spectral images include both multispectral images, which contain dozens of bands, and hyperspectral images, which include hundreds of bands. In both cases, these images provide detailed information on the reflectance or emission of materials at different wavelengths [12].

Various investigations have been carried out in the field of spectral imaging. Thus, in [13], models supported by convolutional neural networks were used for the detection of asbestos-cement on RGB and NIR aerial images, achieving detection accuracies of 89%, validating the usefulness of these methods in large-scale inventories. Similarly, in [14], quantitative mapping of asbestos-cement roofs was performed in an extensive mountainous region of the Italian Alps spanning 3263 km using multispectral images obtained from the MVIDIS sensor, achieving a detection precision of 80% and concluding that the spatial resolution of the data constitutes the main source of errors in detection. On the other hand, in [15]-[17], hyperspectral images in the SWIR range (1100-2500 nm) were utilized for asbestos detection in cement matrices, employing models such as SIMCA and PLS-DA, demonstrating high sensitivity and specificity (0.89–1.00) in detection. Likewise, in [18], the use of Mask R-CNN with multispectral satellite images (MSSI) and high-resolution aerial images (HRAI) was evaluated for detecting fiber-cement roofs in Australian residential buildings, obtaining a detection accuracy of 94% and a confidence threshold of 99.8%. Furthermore, in [19], hyperspectral images and ENVI software were used for the mapping and diagnosis of the condition of asbestos-cement roofs in the urban area of Cartagena de Indias, identifying that up to 47% of the surface of some neighborhoods was covered by this material, with an average of 20% at the neighborhood level and more than 9 km² throughout the city. In this same sense, in [20], the effectiveness of a computational method based on the identification of prominent peaks in the spectral curve of asbestos-cement was evaluated, assessing said method effectively with 380-band hyperspectral images from Cartagena de Indias.

Now, regarding the challenges of hyperspectral images, it's notable, first, that by containing hundreds of spectral bands, they generate data cubes with a large volume of information that complicates their analysis. For this reason, in memory-limited environments, processing often requires the use of efficient partitioning and storage techniques [21]-[23]. Likewise, processing these images with complex methods, such as deep learning, demands significant computational power and cost, making their use unsuitable for real-time monitoring applications [24]-[26]. Thus, in this context, it's necessary to have lighter models or utilize dimensionality reduction techniques to balance detection accuracy and speed [27], [28]. In this same sense, concerning multispectral images, given that the number of bands is reduced compared to hyperspectral images, accurately identifying materials with similar spectral signatures becomes challenging [29]-[31]. In this same vein, using multispectral images makes the identification of materials in complex

mixtures or superimposed layers difficult, as the spectral signature can be a combination of various materials [29].

Considering the challenges in processing and analyzing the large amount of data contained in hyperspectral images, and the challenge of multispectral images in enabling material detection with fewer bands, this article proposes, as a first contribution, the evaluation of methods based on spectral similarity (correlation (CBS), spectral differential similarity (SDS), Euclidean distance (EDS)) and Artificial Neural Networks (ANN) for the detection of asbestos-cement in 4-band NIR multispectral images from the city of Cartagena de Indias. Likewise, this work proposes evaluating these four methods on a new version of the images, where a new band or layer corresponding to the PCA (Principal Component Analysis) principal component of the image was added, in order to identify if there's an improvement in the detection capabilities of each evaluated method.

Thus, given the lower economic cost of acquiring NIR images, as well as their lower computational processing cost, this work presents a competitive alternative for identifying roofs with asbestos, which is of great interest to governmental authorities in Colombia and other developing countries for mitigating the harmful effects of this material on human health. Furthermore, this work aims to be replicated and extrapolated at academic and business levels regarding the evaluation of these methods for detecting other materials, leveraging the technique of enriching the NIR image with a fifth band derived from the PCA principal component.

Recent studies have explored lightweight convolutional neural networks (CNNs), support vector machines (SVMs) and classical spectral angle-based methods such as SAM and SID for roof material detection and general multispectral classification. Lightweight CNNs often achieve strong performance with spatial context, but they depend on larger annotated datasets, data augmentation and GPU-oriented training pipelines [32], [33].

SVMs have also been widely applied to multispectral and hyperspectral classification due to their robustness with small sample sizes, although they typically require careful parameter tuning and do not provide explicit spectral interpretability [34]. SAM and SID remain popular reference methods because of their stability and well-understood spectral behavior, yet their performance tends to decline when the number of available spectral bands is limited [35].

Independent validation is also common in remote sensing applications, especially when ground-truth reliability is uncertain. These strategies often rely on field surveys, ancillary cadastral layers or high-resolution reference imagery to cross-check roof materials or land cover types [36]. For this reason, the dataset was carefully curated through visual inspection and controlled sampling to ensure internal consistency and interpretability.

Within this landscape, the present work contributes by systematically comparing three spectral similarity measures (CBS, SDS and EDS) against a simple artificial neural network using only four spectral bands and a PCA-derived component. This comparison offers a realistic baseline for low-band multispectral scenarios where high-end hyperspectral sensors, extensive ground truth or GPU-heavy architectures are not feasible.

In recent studies on roof material detection, most approaches rely on hyperspectral sensors or computationally intensive models such as CNN-based architectures and high-dimensional spectral classifiers. These methods require large datasets, specialized acquisition systems or GPU-oriented processing pipelines. In contrast, the present work focuses on a lightweight and low-band multispectral setting using only four spectral bands (R, G, B and NIR) and an additional PCA-derived component.

The contribution lies in comparing three spectral similarity measures (CBS, SDS and EDS) against a simple artificial neural network, while using a small and fully interpretable dataset collected from real urban structures. The study underscores computational efficiency, reproducibility, and the practical feasibility of deploying these methods within low-cost monitoring workflows where high-end hyperspectral sensors are not available—an aspect particularly relevant for developing countries such as Colombia, where asbestos has been recently banned and large-scale asbestos-cement roof assessment is urgently needed.

The remainder of the article is organized as follows: Section 2 presents the methodological phases that guided the development of this research. In Section 3, the results derived from this investigation are presented, which initially includes the adjustment and evaluation of the detection capabilities of the four methods using sample spectral signatures of asbestos-cement and other materials derived from 4-band and 5-band images. Additionally, the deployment of the four methods on a NIR image of areas adjacent to La Popa hill in Cartagena is included, visually verifying the zones detected by each method. Furthermore, the evaluation of each method's computational efficiency in processing and analyzing a 30x30 pixel region of the image, where each pixel has five spectral bands, is also

included. Finally, Section 4 contains the conclusions and future work derived from this research.

2. METHODOLOGY

For this research, a four-phase adaptation of the CRISP-DM methodology was implemented: P1. Business and data understanding, P2. Data preparation, P3. Modeling and evaluation, and P4. Deployment of models (see Figure 1).

The CRISP-DM methodology was chosen because its clear structure, with standardized phases, facilitates the organization and comprehension of data science project lifecycles, enabling clear management from problem understanding to model implementation, deployment, and maintenance [37]-[39].

Moreover, it's worth noting that the CRISP-DM methodology is highly adaptable and can be integrated with agile approaches or customized for specific application contexts, such as computer vision [40].

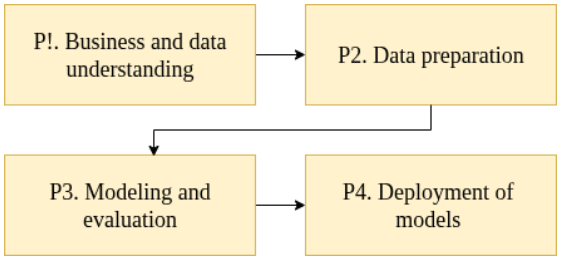

***Fig. 1**. Considered methodology.*
***Source:** own elaboration.*

In Phase 1 of the methodology, based on a reference aerial multispectral image of 3000 × 3000 pixels and four spectral reflectance bands (red, green, blue, and near-infrared), a total of 600 pixels or sample spectral signatures were selected through visual inspection and field validation, of which 300 corresponded to asbestos–cement roofing materials and 300 to other materials. Likewise, the multispectral aerial images used in this study were obtained from publicly accessible datasets published by the Cartagena Public Environmental Authority (EPA), and although their spatial coverage encompasses the entire urban area of the city, the analysis was specifically focused on the region corresponding to Cerro de La Popa.

According to the technical information associated with the published data, the images had previously undergone spatial resampling and radiometric correction processes; therefore, the analysis was carried out directly using the standardized spatial resolution and the corrected radiometric values provided in the dataset. In the same manner, the described procedure was also applied to an equivalent image composed of five spectral bands, where the fifth incorporated band was obtained from the first principal component derived from the application of principal component analysis (PCA) to the original four-band image.

It is worth noting that the image preprocessing consisted of converting the source files into a structured multispectral data cube, removing evident outlier values, and independently normalizing each spectral band in order to reduce variability associated with illumination conditions. As previously mentioned, a five-band version of the dataset was also generated by computing and incorporating the normalized first principal component obtained from the application of principal component analysis (PCA). These procedures ensured consistent input representations for both the spectral similarity measures and the artificial neural network model. Given the absence of absolute radiometric calibration records, the study focuses on the analysis of relative spectral behavior rather than absolute reflectance values.

The selection of the 600 spectral signatures used in this work followed a structured procedure validated through field verification. In this regard, the identification of asbestos–cement (AC) roofing materials was based on a methodological framework adapted from previous studies [41] and adjusted to the pecific characteristics of the analyzed dataset. In that previous study, conducted in the urban area of Cartagena, physical roofing samples (1 × 1 cm) were collected from representative buildings and subsequently analyzed using polarized light microscopy (PLM), in accordance with ASTM D7521-22, in order to confirm the presence of asbestos fibers.

These verified asbestos–cement roofs served as reference locations for spectral characterization and class labeling in the present study. Likewise, the remaining roof material classes were delineated through detailed visual interpretation and field verification. Each sampled roof was georeferenced using GPS coordinates and, when available, supported by auxiliary cadastral information, such as parcel boundaries and building footprints, with the aim of ensuring the spatial and material consistency of the samples.

The same set of spatial locations was used for both the four-band and five-band datasets in order to preserve consistency between experiments. In this way, during Phase 1 two independent datasets were constructed, one corresponding to the four-band image and the other to the five-band image, each composed of 300 sample pixels and subdivided into two classes: asbestos–cement and other materials. The stability of the spectral responses and the low noise levels present in the images enabled the extraction of consistent and

reproducible spectral signatures for subsequent analysis.

These sample pixels or spectral signatures were used to calibrate and evaluate the four methods considered in this article, with the aim of identifying the detection capability of each method and, in the case of spectral similarity methods, determining the reference thresholds from which the material is detected. It is worth noting that, for the conversion of the image from TIFF format to a data cube or three-dimensional array, the capabilities of the Python rasterio library were leveraged, as it allows the original data cube to be converted into a multidimensional array compatible with the Python NumPy library.

Based on the above, Figure 2 presents, on an RGB representation of the multispectral image of areas adjacent to La Popa hill, the location of the selected sample pixels, where asbestos-cement pixels are shown in blue and other material pixels are shown in red.

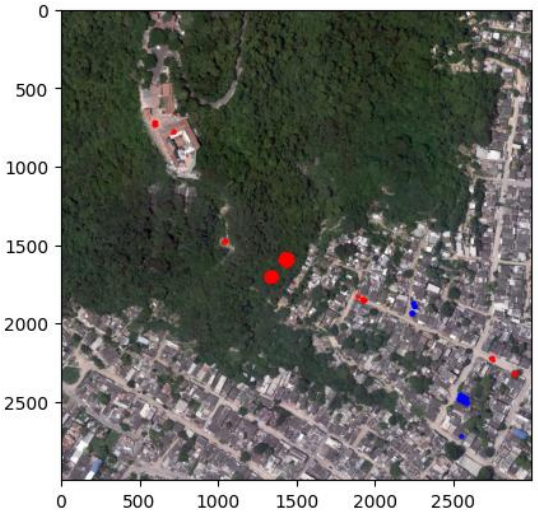

***Fig. 2**. Asbestos-cement and other material sample pixels*
***Source:** own elaboration.*

In this same sense, in Figure 3, the 50 spectral signatures of asbestos-cement and the 50 signatures of other materials, obtained from the 4-band spectral image, are presented based on the 100 reference points.

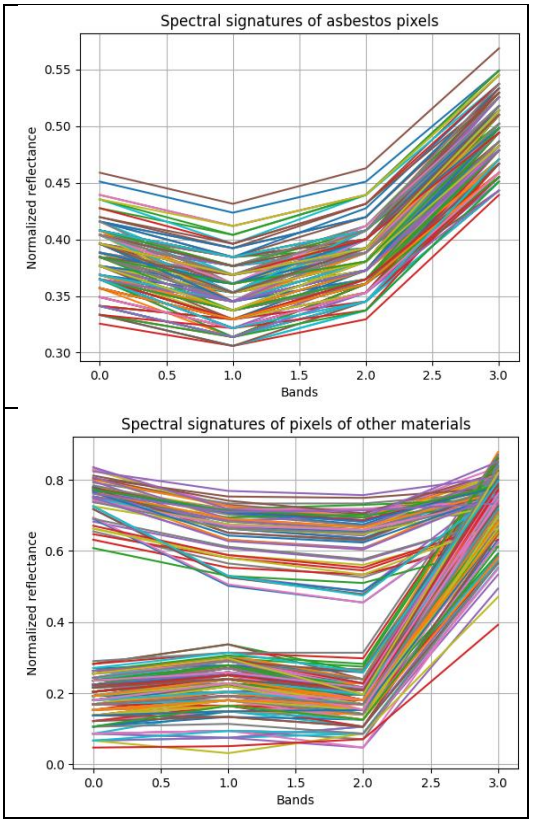

***Fig. 3**. Spectral signatures of the 4-band pixels.*
***Source:** own elaboration.*

Furthermore, in Figure 4, the 300 spectral signatures of asbestos-cement and the 300 signatures of other materials, obtained from the 5-band spectral image, are presented using the same 600 sample points.

Additionally, in Phase 2 of the methodology, for the three methods based on spectral similarity, the average spectral signatures or characteristic spectral signatures associated with the 4-band and 5-band asbestos-cement sample pixels were calculated.

This was achieved by leveraging the capabilities of the NumPy library, which allows for band-by-band calculation of the average reflectance, thus yielding the two average spectral signatures for 4 and 5 bands, respectively.

The two signatures were subsequently used to calculate the similarity with the two groups of sample pixels and to determine the detection thresholds and the detection capability of the spectral similarity methods. Now, regarding the Artificial Neural Network (ANN) model, two datasets were formed by labeling the 4-band and 5-band sample spectral signatures, respectively.

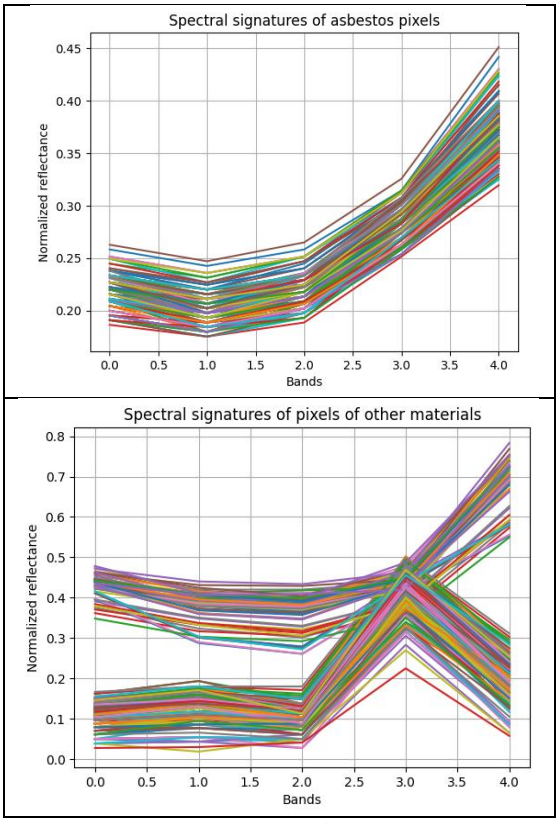

Fig. 4*. Spectral signatures of the 5-band pixels.*
Source: *own elaboration.*

Consequently, the resulting datasets were composed of 300 records associated with asbestos–cement sample signatures labeled as 1 and 300 records associated with sample signatures of other materials labeled as 0. The constructed dataset was used for the training and evaluation of the ANN model.

For the ANN model, the dataset was divided into a training set and a test set following a 70/30 split. Given the limited number of samples, the ANN was included only as a lightweight baseline rather than as a fully generalizable classifier. No cross-validation scheme was applied, since the objective of the study was not to optimize a high-capacity learning model but to compare its behavior with the spectral similarity methods under the same reduced input conditions.

It is worth additionally mentioning that although selecting 300 asbestos–cement samples may appear to be a limitation, these points belong to the same material and therefore exhibit a very similar spectral signature, which makes it unnecessary to collect thousands of samples of this material. However, one of the possible limitations of the study is the identification, through field visits, of appropriate areas where the material is present and proper samples can be obtained.

Likewise, in Phase 3 of the methodology, the three similarity methods based on correlation, spectral differential similarity, and Euclidean distance were first implemented and evaluated with both the 4-band and 5-band sample pixel groups. This was done to identify each method's detection capability and, consequently, the minimum detection thresholds, by verifying that the minimum similarity percentage with asbestos-cement pixels was higher than the maximum similarity percentage with other materials.

The thresholds are crucial for use in deploying the spectral similarity methods over the entire image, allowing them to indicate the levels at which these methods classify pixels as asbestos-cement. Specifically, the mathematical equation representing correlation-based similarity (CBS), which was implemented in this phase, is presented in (1), where 'r' is the normalized Pearson correlation. When calculated by Python's SciPy library, this value ranges from 0 to 2 and determines the degree of similarity between the patterns or trends of two arrays, in this case, the correlated spectral pixels.

$$CBS = (\frac{r+1}{2})x100 \quad (1)$$

Likewise, Equation (2) represents the spectral differential similarity (SDS), where Xi and Yi correspond to the two compared arrays, being in this case the average pixel and a specific pixel from the image. For its part, N corresponds to the number of bands in the image, in this case 4 or 5. Thus, the SDS calculates the sum of the band-by-band differences in reflectances of the two arrays, such that the smaller the difference, the more similar the compared arrays or spectral signatures.

$$SDS = 100 - (\frac{\sum (X_i - Y_i)}{N})x100 \ (2)$$

Additionally, Equation (3) represents the spectral similarity based on the Euclidean Distance (EDS), where Xi and Yi are the compared and previously normalized arrays, while ED is the normalized Euclidean distance between arrays Xi and Yi. The ED measures the straight-line distance between two spectral arrays in an N-dimensional space, where N is the number of spectral bands.

$$EDS = \left(1 - \frac{ED(Xi,Yi)}{\sqrt{2}}\right) x\ 100 \quad (3)$$

Now, concerning the ANN model, in this phase, the architecture of the models to be applied to the 4-band and 5-band datasets was designed and implemented using Python's TensorFlow library. Their performance was evaluated over 100 epochs, with accuracy taken as the reference metric. It's worth mentioning that the architectures were iteratively evaluated until the most consistent and best-performing results were obtained on both the training and test sets. Specifically,

Equation (3) mathematically represents the architecture of the Artificial Neural Network (ANN), where Xi represents the neuron's inputs, wi corresponds to the weights associated with each input, b is the bias term, f is the activation function (such as ReLU, tanh, sigmoid), and $\hat{y}$ is the estimated output generated by the neuron.

$$\hat{y} = f\left(\sum_{i=1}^{n} \omega_i x_i + b\right) \quad (3)$$

Finally, once each method's fitting capability was identified, in Phase 4 of the methodology, each of the four considered methods was deployed on the 4-band and 5-band reflectance multispectral images. This was done using the thresholds detected in Phase 3 for the spectral similarity methods, in order to obtain the percentage of asbestos-cement for each method and visually compare the detected areas in each case.

Additionally, in this phase, the computational efficiency of each method was compared by executing them on a 30x30 pixel, 5-band reflectance image region over a varying number of repetitions: 25, 50, 75, and 100. This was done to obtain the average processing time per repetition and the total average processing time, which was then used to evaluate the relative computational efficiency among the methods.

To ensure that the timing results were not affected by single-run variability, each method was executed multiple times over the same 30×30-pixel, five-band image region. Four repetition levels were used (25, 50, 75 and 100 runs), and the reported values correspond to the average processing time across repetitions.

This repetition scheme provides a basic measure of temporal stability even though no confidence intervals are reported, as the primary goal of this experiment was to compare the relative efficiency of the methods rather than to conduct a full statistical performance analysis.

All experiments were conducted in an academic computing environment using Google Colab, running on a Linux-based operating system with 12.7 GB of available RAM. No GPU acceleration was used. This description of the execution environment is provided to contextualize the timing comparisons, which reflect relative differences between methods rather than absolute execution times.

Processing times were measured using Python's built-in time module, which records the wall-clock duration required for each execution. Only the core computation of each algorithm was included in the measurement; data loading and preprocessing were excluded to avoid biasing the comparison.

3. RESULTS AND DISCUSSION

At the results level, first, the average spectral signatures of the asbestos-cement sample pixels for both 4 and 5 bands were obtained; these are presented in Figure 5. These signatures were used to evaluate the asbestos-cement detection capability of the three spectral similarity methods across both groups of 4-band and 5-band reflectance sample pixels.

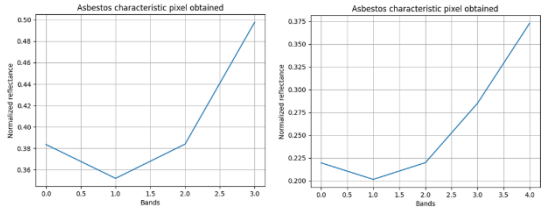

***Fig. 5**. Average spectral signature obtained for the 4-band and 5-band sample pixels.*
***Source:** own elaboration.*

Likewise, concerning the ANN model, two datasets of 100 instances were structured, each associated with the 4-band and 5-band sample pixels. Thus, the first dataset comprises 600 instances with five columns: the first four corresponding to the reflectance values (RGB and NIR bands), and the last column corresponding to the label associated with the pixel type '1' for asbestos-cement pixels and '0' for other material pixels. Similarly, the second dataset was composed of six columns: the first five columns corresponded to the reflectance values of the four bands from the first dataset plus an additional band associated with the first principal component of PCA applied to the image. Furthermore, the sixth column corresponds to the label associated with the pixel type, similar to the first dataset. Consequently, Figure 6 illustrates the structure of the second dataset, which, as mentioned, includes an additional band alongside the information from the first dataset.

	band1	band2	band3	band4	pixel
0	0.396078	0.352941	0.380392	0.513725	1.0
1	0.407843	0.360784	0.380392	0.509804	1.0
2	0.396078	0.368627	0.400000	0.517647	1.0
3	0.403922	0.352941	0.380392	0.501961	1.0
4	0.403922	0.368627	0.400000	0.513725	1.0
...	...	...	...	...	...
595	0.215686	0.239216	0.207843	0.800000	0.0
596	0.180392	0.227451	0.152941	0.745098	0.0
597	0.168627	0.192157	0.168627	0.713725	0.0
598	0.254902	0.298039	0.196078	0.819608	0.0
599	0.270588	0.313725	0.258824	0.796078	0.0

600 rows × 5 columns

***Fig. 6**. Dataset obtained for the 5-band image.*
***Source:** own elaboration.*

Now, based on the average spectral signatures obtained from the 4-band and 5-band asbestos-cement sample pixels, the three considered spectral similarity methods (CBS, SDS, and EDS) were implemented and evaluated. In these evaluations, the similarity of the characteristic 4-band and 5-band spectral signatures to the two groups of sample pixels was determined in three different mathematical ways.

As previously mentioned, the three methods were implemented leveraging the advantages provided by the SciPy and NumPy libraries for mathematical operations between arrays. Thus, in Figure 7, the comparative results obtained by the three spectral similarity methods with the two groups of 4-band reflectance pixels are presented.

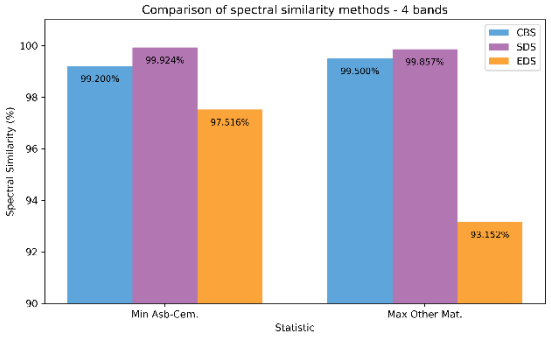

***Fig. 7**. Comparison of spectral similarity methods with 4-Band sample pixels.*
***Source:** own elaboration.*

According to the results presented in Figure 7, it can be observed that for the four-band sample pixels, the only method that exhibits overlap is CBS, meaning that the minimum percentage of spectral similarity with the 300 asbestos–cement sample pixels is not greater than the maximum similarity percentage with pixels corresponding to other materials.

Likewise, it is observed that the SDS and EDS methods do not present overlap and allow a clearer differentiation of the characteristic spectral signature of asbestos–cement from those of other materials, such that the difference between thresholds is 0.067% for SDS and 4.364% for EDS. In this sense, it can also be observed that, although the SDS method exhibits the highest minimum similarity percentage among the group, the EDS method provides the greatest differentiation of the spectral signature with respect to the sample pixels of other materials.

On the other hand, Figure 8 presents the comparative results obtained by the three spectral similarity methods using the two groups of five-band reflectance pixels, where it can be observed that, unlike the evaluation performed with the four-band sample pixels, none of the three considered methods exhibits overlap; that is, in all three cases the minimum similarity with asbestos–cement pixels is greater than the maximum similarity with pixels corresponding to other materials. Likewise, it is possible to observe that, for the CBS method, the difference between the two thresholds changed from being negative to reaching 2.3%, whereas for the SDS and EDS methods the difference decreased slightly, respectively from 0.067% to 0.027% and from 4.364% to 3.479%. Thus, although the inclusion of the additional band slightly reduces the detection capability of the SDS and EDS methods, the CBS method allows a clear differentiation of the characteristic spectral signature of pixels associated with other materials, achieving a threshold difference of 2.3%.

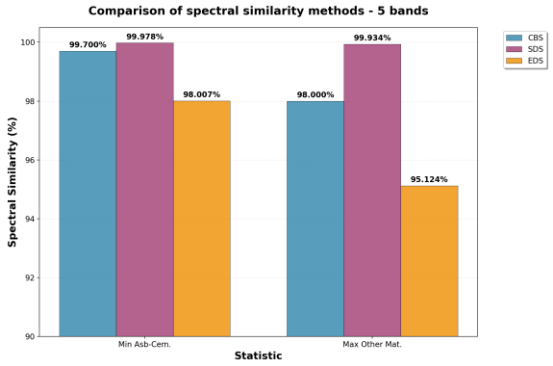

***Fig. 8**. Comparison of spectral similarity methods with 5-Band sample pixels.*
***Source:** own elaboration.*

Based on the foregoing, although the correlation method improved with the 5 bands in its ability to differentiate the spectral signature of asbestos-cement from pixels of other materials, the EDS method continues to exhibit a greater difference in thresholds and, therefore, provides the best detection capability with the sample pixels.

Now, continuing with the ANN model, the architecture was designed and fitted using the training and test sets derived from the 4-band reflectance dataset. It was found that the best fit occurred when the sequential model was structured with an input layer of 4 neurons, an output layer of 1 neuron due to the binary nature of the problem, and three hidden layers of 12, 8, and 4 neurons. ReLU activation functions were utilized in the hidden layers, and a Sigmoid function was employed in the output layer.

For regularization, a Dropout layer with a 20% rate was applied after each layer, including the input and hidden layers, to prevent overfitting. The model was compiled using the Adam optimizer with a learning rate of 0.001, and 'binary_crossentropy' was employed as the loss function, which is suitable for binary classification, along with 'accuracy' as the performance metric. Thus, in Figure 9, the structure of the ANN model and the TensorFlow implementation code are presented.

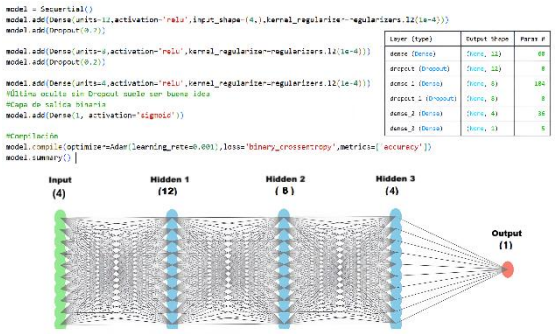

***Fig. 8**. ANN structure for the 4-band spectral dataset.*
***Source:** own elaboration.*

In the same manner, for the five-band dataset a similar structure was obtained for the ANN model, such that in this case an input layer with five neurons and an output layer with a single neuron were defined, given the binary nature of the problem, along with three hidden layers comprising 12, 8, and 4 neurons, while keeping all other parameters and functions identical to those used in the ANN model for the four-band dataset.

The models' structure was iteratively evaluated over 100 epochs with the training and test sets from the 4-band and 5-band datasets. Thus, for the ANN model associated with the 4-band dataset and presented in Figure 8, both the performance, based on the accuracy metric, and the losses across different epochs in both training and evaluation were obtained, as shown in Figure 9.

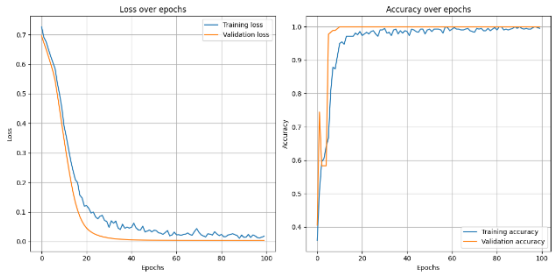

***Fig. 9**. ANN model performance with the 4-band dataset.*
***Source:** own elaboration.*

From Figure 9, it can be observed that the training loss shows a pronounced decrease during the initial epochs, progressively stabilizing at values close to 0.05 from approximately epoch 40 onward, with slight oscillations inherent to the optimization process. Similarly, the validation loss decreases consistently and remains at comparable values, slightly lower than those of the training loss, suggesting adequate model convergence without evidence of overfitting.

Regarding the accuracy metric, the training accuracy increases rapidly and reaches values above 0.95 within the first 15–20 epochs, subsequently stabilizing near 1.0. The validation accuracy follows a very similar trend, reaching values close to unity at early stages of training, which indicates a high level of performance and a notable generalization capability of the ANN model on the evaluated four-band dataset.

Likewise, regarding the evaluation of the 5-band ANN model, Figure 10 presents the results for the model's losses and performance over 100 epochs on both the training and test sets.

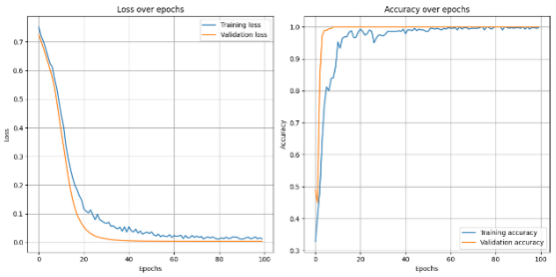

***Fig. 10**. ANN model performance with the 5-band dataset.*
***Source:** own elaboration.*

According to Figure 10, it can be observed that the training loss of the ANN model trained with the five-band spectral dataset exhibits a rapid and pronounced decrease during the initial epochs, progressively stabilizing at values close to 0.03–0.05 from approximately epochs 35–40 onward, with slight oscillations associated with the iterative optimization process. Consistently, the validation loss follows a similar trend, reaching values slightly lower than those of the training loss and remaining stable throughout training, which suggests adequate model convergence without indications of overfitting.

With respect to the accuracy metric, the training accuracy increases rapidly and exceeds 0.95 within the first 15–20 epochs, subsequently stabilizing at values close to unity. The validation accuracy exhibits an almost identical behavior, reaching values close to 1.0 at early stages of training, which evidences a high level of performance and a remarkable generalization capability of the ANN model when incorporating additional spectral information in the five-band dataset.

Thus, in comparison with the model trained using the four-band dataset, the inclusion of the additional band results in slightly faster convergence and greater stability in both loss and accuracy, suggesting a marginal benefit in the model learning process.

In this same sense, Figure 11 presents the average performance achieved by the ANN model over the last 20 epochs of the 100 considered, in terms of the metrics derived from the confusion matrix, such as precision, recall, and F1-score, for both the four-band dataset and the five-band dataset.

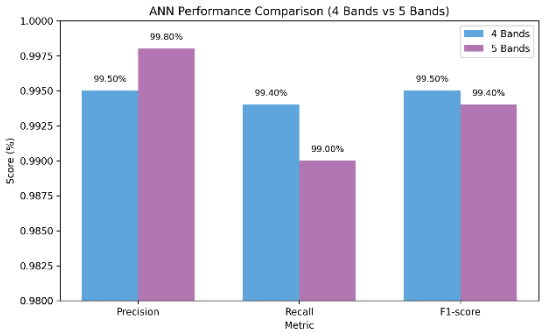

***Fig. 11**. Performance metrics of the ANN model for the four-band and five-band datasets.*
***Fuente:** own elaboration.*

Based on the results presented in Figure 11, it can be observed that the three considered metrics (precision, recall, and F1-score) reach values above 99% in both datasets, which evidences a globally high and consistent performance of the evaluated models. In particular, the ANN model trained with the four-band dataset exhibits slightly superior performance in the recall and F1-score metrics, suggesting a greater ability to correctly identify the target class and a better balance between precision and completeness.

On the other hand, the ANN model evaluated on the five-band dataset shows superior performance in the precision metric, indicating a reduction in the proportion of false positives, possibly associated with the incorporation of additional spectral information. Nevertheless, the observed differences between both configurations are marginal, which suggests that the ANN model maintains robust behavior with respect to variations in the number of considered spectral bands.

Now, to deploy the three spectral similarity methods and the sequential ANN model across the entire 4-band multispectral image, an iteration was performed for each pixel. Subsequently, each pixel was classified within an RGB representation of the multispectral image, following the application of similarity and classification operations using the four methods. Thus, in Figure 11, the asbestos pixels detected by each of the four methods are presented in blue on an RGB image representation.

Based on the results presented in Figure 12, it is visually evident that the EDS and CBS methods are the ones that most accurately detect asbestos–cement pixels in the four-band image, detecting percentages of 6.89% and 5.639% of pixels, respectively. Likewise, it is observed that although the SDS method detects nearly twice as many pixels (13.083%) as the EDS and CBS methods, this method commits more detection errors, identifying asbestos pixels in the upper part of Cerro de La Popa, where the presence of asbestos–cement is not evidenced. Similarly, this method shows greater confusion between road and vegetation pixels compared to the CBS and EDS methods. Finally, although the ANN model achieved good performance during training and is the method that detects the largest number of asbestos pixels, with 19.772%, it is also the method that commits the highest number of errors, confusing vegetation and road pixels with asbestos–cement pixels, resulting in the highest percentage of detected asbestos pixels among the four methods.

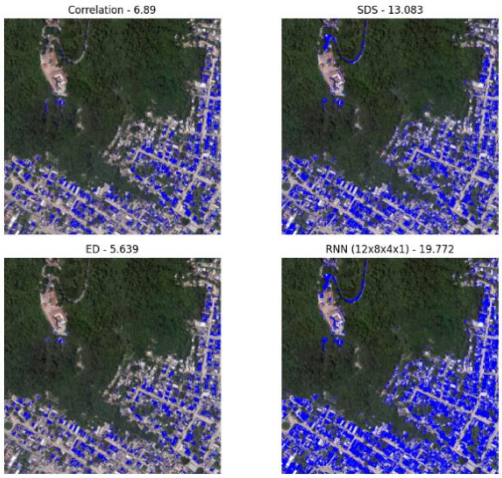

***Fig. 12**. Deployment of the four methods on the 4-band multispectral image.*
***Source:** own elaboration.*

Now, upon implementing and deploying the four considered methods on the 5-band multispectral image (four reflectance bands and an additional band obtained from PCA analysis), the asbestos-cement pixels were classified. Thus, in Figure 12, the detected asbestos-cement pixels are presented in blue on an RGB representation of the image, utilizing the four considered methods.

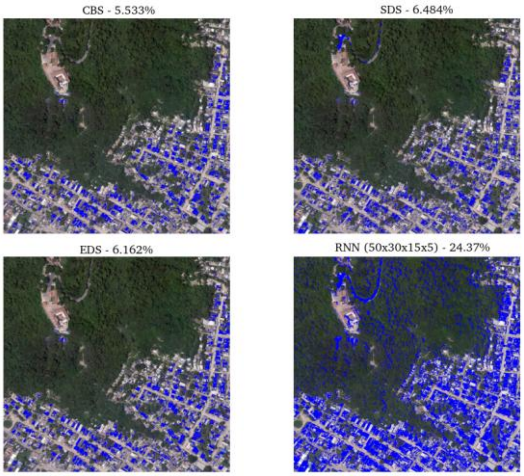

***Fig. 13** Deployment of the four methods on the 5-band multispectral image.*
***Source:** own elaboration.*

According to the results presented in Figure 13, it can be observed that the EDS and CBS methods continue to exhibit the best detection performance, with a slight increase in the detection percentage for the EDS method and a slight decrease for the CBS method, relative to the detection performed on the four-band image. Likewise, with regard to the SDS method, a slightly higher detection percentage was obtained compared to the results achieved with the four-band image; however, errors persist in the upper part of Cerro de La Popa, as well as confusion in vegetation and road pixels. Similarly, with respect to the ANN model, it was found that the detection percentage decreased slightly compared to the four-band image, while detection errors were reduced and, consequently, confusion between vegetation and road pixels with asbestos–cement pixels was diminished. Thus, through the inclusion of an additional band to the four-band image, the CBS and ANN methods refine detection, whereas the EDS method yields comparable detection results and the SDS method slightly reduces its detection capability by increasing the number of errors.

Now, to comparatively evaluate the computational efficiency of the four considered methods, they were deployed in multiple repetitions (25, 50, 75, and 100) on a 30x30 pixel region with 5 spectral bands. This was achieved using Python's timeit library to identify the processing time per repetition, the average processing time, and the relative efficiency of the methods. Thus, Figure 14 presents a line diagram illustrating the processing time obtained by each method across the different repetitions.

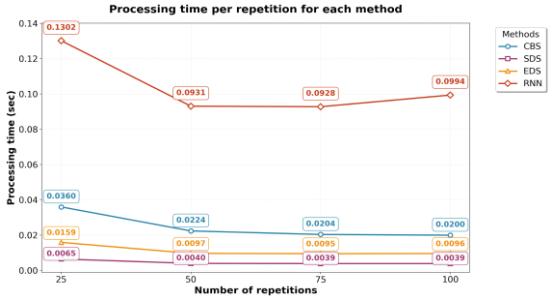

Fig. 14. *Comparison of the computational efficiency of the four methods.*
Source: *own elaboration.*

From the results presented in Figure 13, it's possible to observe how the ANN model, on average, utilizes the most time across the different repetitions. Specifically, to process the 30x30 pixel image with 5 reflectance bands, a minimum time of 92.8 milliseconds and a maximum time of 130.2 milliseconds are employed. Furthermore, regarding the spectral similarity methods, the SDS method is, on average, the most efficient, followed closely by the EDS method, and with a larger difference by the CBS method. No overlap is observed in the curves of these three methods, indicating that the SDS method consistently shows shorter times than the EDS method across different repetitions, and, in turn, the EDS method shows shorter times than the CBS method across different repetitions. Given that the methods with the highest detection efficacy were EDS and CBS, it's important to compare their relative efficiency. Initially, it's noted that the EDS method typically employs processing times for the image region ranging between 9.5 and 15.9 milliseconds, while the CBS method typically uses processing times ranging between 20 and 36 milliseconds. Now, when comparing the overall average across different repetitions for the EDS and CBS methods, it is found that, on average, the CBS method is 2.22 times slower than the EDS method, indicating that in terms of time reduction, the EDS method reduces the time employed by the CBS method by 54.76%.

Now, with regard to the discussion of the obtained results, it is worth noting that this work evaluated the feasibility of using spectral similarity methods and sequential neural network–based approaches for the identification of asbestos–cement roofing materials in four-band multispectral images (RGB + NIR) and in NIR images enriched with a fifth band corresponding to the first PCA component of the image. As a result, it was found that the EDS and CBS methods jointly exhibited the best effectiveness and efficiency in detection.

Thus, in comparison with previous studies, such as 15], [16], [17], which are based on the use of hyperspectral imagery in the shortwave infrared (SWIR) range, the results obtained in this work demonstrate the potential of multispectral data with a low number of bands as a simpler alternative for exploratory material detection. In this way, this approach represents a relevant contribution with respect to prior research focused on asbestos–cement detection using hyperspectral imagery, by demonstrating that the use of four- or five-band images allows a significant reduction in both the computational processing costs and the costs associated with data acquisition, compared to those required to capture and process images composed of hundreds of spectral bands. In this sense, the methods that exhibited the highest effectiveness and efficiency in this study show strong potential to be integrated into near–real-time monitoring environments for asbestos–cement or other materials of environmental interest, particularly in scenarios where access to hyperspectral sensors is limited or unfeasible.

Despite the above, these findings should be interpreted in light of the geographic and environmental context in which the experiments were conducted. The study is based on data from a single region, characterized by specific surface features and atmospheric conditions, as well as by image properties inherent to the available

dataset. Consequently, the obtained results reflect the methodological feasibility of the proposed approach under these particular circumstances rather than a fully generalizable performance. Any large-scale application, whether in operational monitoring contexts or using different types of sensors and environmental configurations, should therefore be considered preliminary and subject to additional validation processes using more diverse datasets and independent reference data.

In this same sense, through the use in the present research of techniques and technologies supported by open-source tools such as rasterio, NumPy, pandas, matplotlib, and TensorFlow, this work becomes a reference that can be replicated and extrapolated by universities and research centers for the detection of different materials in multispectral images, representing a contribution toward mitigating the high costs associated with proprietary image-processing tools such as ENVI. Likewise, the use of these tools facilitates the straightforward customization and hybridization of different methods or approaches, a process that is considerably more complex to implement using proprietary software solutions.

Finally, with regard to the limitations of this research, it should be noted that enriching the four-band image requires first obtaining the additional layer through PCA, which entails additional multispectral image preprocessing time; therefore, this aspect must be considered when adapting this approach to real-time monitoring applications. Despite this, it was observed that the integration of the five bands enables the EDS and CBS methods to achieve more refined results compared to those obtained using the four-band image.

4. CONCLUSIONS AND FUTURE WORK

Considering that, although hyperspectral images pose a computational cost challenge due to their high dimensionality, this article proposes as a contribution the implementation and evaluation of spectral similarity–based methods and RNN models for the detection of asbestos–cement in four- and five-band multispectral images, with the aim of determining the effectiveness of each method in detecting this material using significantly fewer reflectance bands.

The obtained results made it possible to determine that the EDS and CBS methods successfully detected asbestos–cement areas in the multispectral image with good accuracy. These results indicate that this research and the considered methods can be extrapolated to the detection of other materials, representing an alternative to the acquisition and processing costs associated with hyperspectral imagery.

With regard to the limitations of the present research, enriching the four-band image through the incorporation of a component derived from principal component analysis (PCA) requires an additional preprocessing stage, which entails an increase in computational time that must be considered when adapting the approach to real-time processing scenarios. Nevertheless, the inclusion of the fifth band made it possible to improve the stability of the EDS and CBS methods compared to the four-band configuration.

With respect to the computational effectiveness of the evaluated methods, it was found that, for the four-band dataset, the spectral distance methods SDS and EDS did not exhibit overlap in differentiating the characteristic asbestos–cement pixel from sample pixels of other materials, with the EDS method achieving the largest percentage difference between detection thresholds at 4.364%.

In this same sense, although SDS does not present overlap in the thresholds, its percentage difference between thresholds is only 0.067%, which makes it sensitive to classification errors; accordingly, when deployed over the four-band image, it is the spectral distance method that exhibits the highest number of misclassifications. Now, with regard to the results obtained using the five-band dataset, it is important to note that the three spectral distance methods do not present overlap in the differentiation of the characteristic spectral signature with respect to non-asbestos sample pixels, with the CBS and EDS methods showing the highest percentage of threshold differentiation at 2.3% and 3.479%, respectively.

In this way, the inclusion of an additional band contributes to improving the detection capability of the CBS method, while slightly reducing the differentiation threshold of the SDS and EDS methods. Likewise, as observed for the four-band dataset, the SDS method yields comparable results and remains the one that commits the largest number of classification errors among the three spectral distance methods. On the other hand, with respect to the ANN model, although it showed outstanding performance during training and evaluation using the training and test sets for the datasets derived from the four- and five-band images, when the model is deployed over the complete image it exhibits a higher number of classification errors compared to the three spectral distance methods,

such that vegetation and road pixels are confused with asbestos–cement pixels.

With regard to computational efficiency, the four methods considered in this research were deployed over an image region of 50 × 50 pixels with five spectral bands across multiple repetitions (25, 50, 75, and 100). As a result of evaluating the methods over these repeated runs, it was found that the SDS method was the most efficient in processing the image region, with an average processing time of 4.58 milliseconds, whereas the ANN model was the least efficient, with an average processing time of 103.88 milliseconds.

Now, in terms of the methods exhibiting the highest detection effectiveness, the most efficient were EDS and CBS, with respective average processing times of 11.18 milliseconds and 24.7 milliseconds, such that the CBS method is 2.22 times slower than the EDS method. These results allow concluding that both the EDS and CBS methods can be integrated into real-time monitoring systems.

This work presented, as an additional contribution, the use of open-source tools for the preprocessing and detection of asbestos–cement in multispectral images through spectral similarity methods and ANN models, demonstrating that these Python-based libraries and technologies were suitable for the conducted experimentation. Thus, the rasterio library was used to obtain the multidimensional array representing the image. Likewise, the NumPy and SciPy libraries were employed for the implementation, evaluation, and deployment of the three spectral similarity methods.

In this same sense, the TensorFlow library was used for the implementation and evaluation of the ANN model architecture. On the other hand, the timeit library was used to execute multiple repetitions of the four considered methods. Finally, the pandas and matplotlib libraries were used, respectively, to load the points associated with the sample pixels and to generate the plots employed in this research. These tools and technologies can be extrapolated by research centers and universities for the detection of different materials in multispectral images, taking advantage of the customization and hybridization capabilities offered by open-source tools.

As future work derived from the present research, it is intended, in the first instance, to evaluate the effectiveness of machine learning models for the detection of asbestos–cement in four-band multispectral images (including NIR) or five-band images, such as those used in this study. Likewise, it is planned to assess the detection capability of the considered spectral similarity methods on Sentinel-type satellite images with ten spectral bands and a spatial resolution of 10 meters.

ACKNOWLEDGEMENTS

This article is considered a product derived from the project "Formulation of an Integral Strategy to Reduce the Impact on Public and Environmental Health Due to the Presence of Asbestos in the Territory of the Department of Bolívar," financed by the General System of Royalties (SGR) of Colombia and identified with the code BPIN 2020000100366. This project was executed by the University of Cartagena, Colombia, and the Asbestos Free Colombia Foundation.

REFERENCES

[1] C. Zhang, «Introduction to Remote Sensing», en Multi-sensor System Applications in the Everglades Ecosystem, 2020, pp. 31-60. doi: 10.1201/9780429075872-2.

[2] J. Awange, «Fundamentals of Remote Sensing», en Environmental Science and Engineering, 2019, pp. 115-123. doi: 10.1007/978-3-030-03017-9_7.

[3] W. Fu, J. Ma, P. Chen, y F. Chen, «Remote Sensing Satellites for Digital Earth», en Manual of Digital Earth, H. Guo, M. F. Goodchild, y A. Annoni, Eds., Singapore: Springer Singapore, 2020, pp. 55-123. doi: 10.1007/978-981-32-9915-3_3.

[4] B. Zhang et al., «Remotely sensed big data: evolution in model development for information extraction [point of view]», Proc. IEEE, vol. 107, n.o 12, pp. 2294-2301, dic. 2019, doi: 10.1109/jproc.2019.2948454.

[5] Z. Shun et al., «Research on remote sensing image extraction based on deep learning», PeerJ Computer Science, vol. 8, p. e847, ene. 2022, doi: 10.7717/peerj-cs.847.

[6] A. M. Lechner, G. M. Foody, y D. S. Boyd, «Applications in Remote Sensing to Forest Ecology and Management», One Earth, vol. 2, n.o 5, pp. 405-412, may 2020, doi: 10.1016/j.oneear.2020.05.001.

[7] Z. Wang, Y. Ma, Y. Zhang, y J. Shang, «Review of Remote Sensing Applications in Grassland Monitoring», Remote Sensing, vol. 14, n.o 12, p. 2903, jun. 2022, doi: 10.3390/rs14122903.

[8] M. I. Abdulraheem, W. Zhang, S. Li, A. J. Moshayedi, A. A. Farooque, y J. Hu, «Advancement of Remote Sensing for Soil Measurements and Applications: A Comprehensive Review», Sustainability, vol. 15, n.o 21, p. 15444, oct. 2023, doi: 10.3390/su152115444.

[9] P. Wang, X. Ma, y Q. Zhao, «Learning-based classification approach for coded aperture compressive spectral image», en International Conference on Image, Signal Processing, and Pattern Recognition (ISPP 2023), P. Batista y R. Bilas Pachori, Eds., Changsha, China: SPIE, jun. 2023, p. 137. doi: 10.1117/12.2681198.

[10] A. Bodkin, A. Sheinis, A. Norton, J. Daly, S. Beaven, y J. Weinheimer, «Snapshot hyperspectral imaging: the hyperpixel array camera», en SPIE Proceedings, S. S. Shen y P. E. Lewis, Eds., Orlando, Florida, USA: SPIE, may 2009, p. 73340H. doi: 10.1117/12.818929.

[11] L. Demarchi, A. Kania, W. Ciężkowski, H. Piórkowski, Z. Oświecimska-Piasko, y J. Chormański, «Recursive Feature Elimination and Random Forest Classification of Natura 2000 Grasslands in Lowland River Valleys of Poland Based on Airborne Hyperspectral and LiDAR Data Fusion», Remote Sensing, vol. 12, n.o 11, p. 1842, jun. 2020, doi: 10.3390/rs12111842.

[12] D. Hong et al., «SpectralGPT: Spectral Remote Sensing Foundation Model», IEEE Trans. Pattern Anal. Mach. Intell., vol. 46, n.o 8, pp. 5227-5244, ago. 2024, doi: 10.1109/tpami.2024.3362475.

[13] M. Krówczyńska, E. Raczko, N. Staniszewska, y E. Wilk, «Asbestos—Cement Roofing Identification Using Remote Sensing and Convolutional Neural Networks (CNNs)», Remote Sensing, vol. 12, n.o 3, p. 408, ene. 2020, doi: 10.3390/rs12030408.

[14] F. Frassy et al., «Mapping Asbestos-Cement Roofing with Hyperspectral Remote Sensing over a Large Mountain Region of the Italian Western Alps», Sensors, vol. 14, n.o 9, pp. 15900-15913, ago. 2014, doi: 10.3390/s140915900.

[15] G. Bonifazi, G. Capobianco, y S. Serranti, «Asbestos containing materials detection and classification by the use of hyperspectral imaging», Journal of Hazardous Materials, vol. 344, pp. 981-993, feb. 2018, doi: 10.1016/j.jhazmat.2017.11.056.

[16] G. Bonifazi, G. Capobianco, y S. Serranti, «Hyperspectral Imaging and Hierarchical PLS-DA Applied to Asbestos Recognition in Construction and Demolition Waste», Applied Sciences, vol. 9, n.o 21, p. 4587, oct. 2019, doi: 10.3390/app9214587.

[17] O. Trotta, G. Bonifazi, G. Capobianco, y S. Serranti, «DETECTION OF ASBESTOS CONTAINING MATERIAL IN POST-EARTHQUAKE BUILDING WASTE THROUGH HYPERSPECTRAL IMAGING AND MICRO-X-RAY FLUORESCENCE», Detritus, n.o 21, pp. 27-34, dic. 2022, doi: 10.31025/2611-4135/2022.17233.

[18] M. Hikuwai, N. Patorniti, A. Vieira, G. Frangioudakis Khatib, y R. Stewart, «Artificial Intelligence for the Detection of Asbestos Cement Roofing: An Investigation of Multi-Spectral Satellite Imagery and High-Resolution Aerial Imagery», Sustainability, vol. 15, n.o 5, p. 4276, feb. 2023, doi: 10.3390/su15054276.

[19] D. Enrique Valdelamar Martínez, M. Saba, y L. K. Torres Gil, «Assessment of asbestos-cement roof distribution and prioritized intervention approaches through hyperspectral imaging», Heliyon, vol. 10, n.o 3, p. e25612, feb. 2024, doi: 10.1016/j.heliyon.2024.e25612.

[20] G. E. Chanchí-Golondrino, M. A. Ospina-Alarcón, y M. Saba, «Proposal of a computational method for asbestos detection in hyperspectral images based on the identification of prominent peaks in the spectral signature», rev. investig. desarro. innov, vol. 15, n.o 1, pp. 119-138, mar. 2025, doi: 10.19053/uptc.20278306.v15.n1.2025.19183.

[21] B. G. Ram, P. Oduor, C. Igathinathane, K. Howatt, y X. Sun, «A systematic review of hyperspectral imaging in precision agriculture: Analysis of its current state and future prospects», Computers and Electronics in Agriculture, vol. 222, p. 109037, jul. 2024, doi: 10.1016/j.compag.2024.109037.

[22] N. Ghasemi, J. A. Justo, M. Celesti, L. Despoisse, y J. Nieke, «Onboard Processing of Hyperspectral Imagery: Deep Learning Advancements, Methodologies, Challenges, and Emerging Trends», IEEE J. Sel. Top. Appl. Earth Observations Remote Sensing, vol. 18, pp. 4780-4790, 2025, doi: 10.1109/jstars.2025.3527898.

[23] A. C. Toma, S. Panica, D. Zaharie, y D. Petcu, «Computational challenges in processing large hyperspectral images», en 2012 5th Romania Tier 2 Federation Grid, Cloud &

High Performance Computing Science (RQLCG), oct. 2012, pp. 111-114. Accedido: 12 de julio de 2025. [En línea]. Disponible en: https://ieeexplore.ieee.org/document/6528260

[24] S. Li, W. Song, L. Fang, Y. Chen, P. Ghamisi, y J. A. Benediktsson, «Deep Learning for Hyperspectral Image Classification: An Overview», IEEE Trans. Geosci. Remote Sensing, vol. 57, n.o 9, pp. 6690-6709, sep. 2019, doi: 10.1109/tgrs.2019.2907932.

[25] M. E. Paoletti, J. M. Haut, J. Plaza, y A. Plaza, «Deep learning classifiers for hyperspectral imaging: A review», ISPRS Journal of Photogrammetry and Remote Sensing, vol. 158, pp. 279-317, dic. 2019, doi: 10.1016/j.isprsjprs.2019.09.006.

[26] Z. Yu y W. Cui, «LSCA-net: A lightweight spectral convolution attention network for hyperspectral image processing», Computers and Electronics in Agriculture, vol. 215, p. 108382, dic. 2023, doi: 10.1016/j.compag.2023.108382.

[27] U. Ghous, M. S. Sarfraz, M. Ahmad, C. Li, y D. Hong, «EXNet: (2+1)D Extreme Xception Net for Hyperspectral Image Classification», IEEE J. Sel. Top. Appl. Earth Observations Remote Sensing, vol. 17, pp. 5159-5172, 2024, doi: 10.1109/jstars.2024.3362936.

[28] Y.-L. Chang et al., «Consolidated Convolutional Neural Network for Hyperspectral Image Classification», Remote Sensing, vol. 14, n.o 7, p. 1571, mar. 2022, doi: 10.3390/rs14071571.

[29] J. M. Bioucas-Dias et al., «Hyperspectral Unmixing Overview: Geometrical, Statistical, and Sparse Regression-Based Approaches», IEEE J. Sel. Top. Appl. Earth Observations Remote Sensing, vol. 5, n.o 2, pp. 354-379, abr. 2012, doi: 10.1109/jstars.2012.2194696.

[30] X. Huang, P. Wang, S. Zhang, X. Zhao, y Y. Zhang, «Structural health monitoring and material safety with multispectral technique: A review», Journal of Safety Science and Resilience, vol. 3, n.o 1, pp. 48-60, mar. 2022, doi: 10.1016/j.jnlssr.2021.09.004.

[31] L. Wunsch, M. Hubold, R. Nestler, y G. Notni, «Realisation of an Application Specific Multispectral Snapshot-Imaging System Based on Multi-Aperture-Technology and Multispectral Machine Learning Loops», Sensors, vol. 24, n.o 24, p. 7984, dic. 2024, doi: 10.3390/s24247984.

[32] Y. Chen, H. Jiang, C. Li, X. Jia, y P. Ghamisi, «Deep Feature Extraction and Classification of Hyperspectral Images Based on Convolutional Neural Networks», IEEE Trans. Geosci. Remote Sensing, vol. 54, n.o 10, pp. 6232-6251, oct. 2016, doi: 10.1109/TGRS.2016.2584107.

[33] E. Maggiori, Y. Tarabalka, G. Charpiat, y P. Alliez, «Convolutional Neural Networks for Large-Scale Remote-Sensing Image Classification», IEEE Trans. Geosci. Remote Sensing, vol. 55, n.o 2, pp. 645-657, feb. 2017, doi: 10.1109/TGRS.2016.2612821.

[34] F. Melgani y L. Bruzzone, «Classification of hyperspectral remote sensing images with support vector machines», IEEE Trans. Geosci. Remote Sensing, vol. 42, n.o 8, pp. 1778-1790, ago. 2004, doi: 10.1109/TGRS.2004.831865.

[35] R. H. Yuhas, A. F. Goetz, y J. W. Boardman, «Discrimination among semi-arid landscape endmembers using the spectral angle mapper (SAM) algorithm», en JPL, Summaries of the Third Annual JPL Airborne Geoscience Workshop. Volume 1: AVIRIS Workshop, 1992.

[36] N. Audebert, B. Le Saux, y S. Lefèvre, «Beyond RGB: Very high resolution urban remote sensing with multimodal deep networks», ISPRS Journal of Photogrammetry and Remote Sensing, vol. 140, pp. 20-32, jun. 2018, doi: 10.1016/j.isprsjprs.2017.11.011.

[37] F. Martínez-Plumed et al., «CRISP-DM Twenty Years Later: From Data Mining Processes to Data Science Trajectories», IEEE Transactions on Knowledge and Data Engineering, vol. 33, n.o 8, pp. 3048-3061, 2021, doi: https://doi.org/10.1109/TKDE.2019.2962680.

[38] J. Saltz, «CRISP-DM for Data Science: Strengths, Weaknesses and Potential Next Steps», presentado en 2021 IEEE International Conference on Big Data (Big Data), Orlando, FL, USA, 2021. doi: https://doi.org/10.1109/BigData52589.2021.9671634.

[39] C. Schröer, F. Kruse, y J. Gómez, «A Systematic Literature Review on Applying CRISP-DM Process Model.», Procedia Computer Science, vol. 181, pp. 526-534, 2021, doi: https://doi.org/10.1016/j.procs.2021.01.199.

[40] A. M. Shimaoka, R. C. Ferreira, y A. Goldman, «The evolution of CRISP-DM for Data Science: Methods, Processes and Frameworks», Reviews, vol. 4, n.o 1, pp. 28-

43, oct. 2024, doi: 10.5753/reviews.2024.3757.

[41] D. Enrique Valdelamar Martínez, M. Saba, y L. K. Torres Gil, «Assessment of asbestos-cement roof distribution and prioritized intervention approaches through hyperspectral imaging», Heliyon, vol. 10, n.o 3, feb. 2024, doi: 10.1016/j.heliyon.2024.e25612.